Nanoplex Delivery of siRNA and Prodrug Enzyme for Multimodality Image-Guided Molecular Pathway Targeted Cancer Therapy

Cong Li,[†,‡,*] Marie-France Penet,[†] Flonné Wildes,[†] Tomoyo Takagi,[†] Zhihang Chen,[†] Paul T. Winnard, Jr,[†] Dmitri Artemov,[†] and Zaver M. Bhujwalla[†,*]

[†]JHU ICMIC Program, The Russell H. Morgan Department of Radiology and Radiological Science, Johns Hopkins University School of Medicine, Baltimore, Maryland 21205, United States, and [‡]School of Pharmacy, Fudan University, Shanghai 201203, China

ABSTRACT The ability to destroy cancer cells while sparing normal tissue is highly sought after in cancer therapy. Small interfering RNA (siRNA)-mediated silencing of cancer-cell-specific targets and the use of a prodrug enzyme delivered to the tumor to convert a nontoxic prodrug to an active drug are two promising approaches in achieving this goal. Combining both approaches into a single treatment strategy can amplify selective targeting of cancer cells while sparing normal tissue. Noninvasive imaging can assist in optimizing such a strategy by determining effective tumor delivery of the siRNA and prodrug enzyme to time prodrug administration and detecting target down-regulation by siRNA and prodrug conversion by the enzyme. In proof-of-principle studies, we synthesized a nanoplex carrying magnetic resonance imaging (MRI) reporters for *in vivo* detection and optical reporters for microscopy to image the delivery of siRNA and a functional prodrug enzyme in breast tumors and achieve image-guided molecular targeted cancer therapy. siRNA targeting of choline kinase-α (Chk-α), an enzyme significantly up-regulated in aggressive breast cancer cells, was combined with the prodrug enzyme bacterial cytosine deaminase (bCD) that converts the nontoxic prodrug 5-fluorocytosine (5-FC) to cytotoxic 5-fluorouracil (5-FU). *In vivo* MRI and optical imaging showed efficient intratumoral nanoplex delivery. siRNA-mediated down-regulation of Chk-α and the conversion of 5-FC to 5-FU by bCD were detected noninvasively with ^{1}H MR spectroscopic imaging and ^{19}F MR spectroscopy. Combined siRNA and prodrug enzyme activated treatment achieved higher growth delay than either treatment alone. The strategy can be expanded to target multiple pathways with siRNA.

KEYWORDS: molecular imaging · cancer · image-guided siRNA delivery · prodrug enzyme therapy

Combining advances in nanotechnology with molecular biology and imaging is providing exciting new nanomedicine-based strategies for cancer treatment. The ideal cancer therapy would target cancer cells while sparing normal tissue. In most conventional chemotherapies, normal cells are damaged together with cancer cells.[1,2] siRNA-mediated silencing of specific targets[3,4] has significant potential in cancer therapy[5] to down-regulate pathways that are up-regulated in cancer cells but not in normal tissue to achieve cancer-cell-specific treatment. Similarly, prodrug enzyme therapy, where a drug-activating enzyme delivered to the tumor converts a nontoxic prodrug to a cytotoxic drug,[6] is being actively investigated to minimize normal tissue damage.[7,8] A combination of both strategies can be exploited to enhance the effect of conventional chemotherapy against cancer cells and minimize damage to normal tissue.

Imaging can play a key role in several aspects of such a treatment. Since tumor vasculature is typically heterogeneous and chaotic,[9,10] the ability to image the delivery of the siRNA and the prodrug-activating enzyme within the tumor would ascertain effective delivery. Noninvasive detection of target down-regulation and visualization of the prodrug-activating enzyme could be exploited to time prodrug administration to minimize normal tissue damage. Detecting the conversion of the prodrug to the active drug within the tumor would verify that the prodrug enzyme was functional.

We previously synthesized a prototype agent consisting of bCD labeled with multimodal MR and optical imaging reporters.[11] bCD converts a nontoxic prodrug 5-FC to 5-FU.[12] The feasibility of image-guided prodrug enzyme therapy using MRI was demonstrated with this prototype agent. Imaging was used to time prodrug administration, and conversion of 5-FC to 5-FU was dynamically monitored by ^{19}F MRS.[13]

Here, for the first time, in proof-of-principle studies, we developed and evaluated a prototype nanoplex carrying MRI and optical reporters that delivered bCD and siRNA in the ER/PR/Her2-neu negative MDA-MB-231 human breast cancer

*Address correspondence to zaver@mri.jhu.edu, congli@fudan.edu.cn.

Received for review August 27, 2010 and accepted October 11, 2010.

Published online October 19, 2010.
10.1021/nn102187v

xenograft model. Both MRI and optical imaging reporters were used because MRI is routinely used in diagnostic imaging, and preclinical results can be clinically translated. Optical imaging reporters, although not easily clinically translatable, allow characterization of the nanoplex at subcellular resolution with microscopy in cells and tissue and provide *in vivo* corroboration of the MRI data.[14]

We used siRNA targeting Chk-α in our prototype nanoplex. Overexpression of Chk-α has been observed in breast and lung cancer.[15−17] ^{1}H MRS studies have consistently detected an elevation of phosphocholine (PC) and total choline (tCho) containing compounds in several cancers[15,18,19] that are closely related to malignant transformation, invasion, and metastasis.[20−24] Chk is a cytosolic enzyme that catalyzes the phosphorylation of choline to PC,[25] a precursor as well as a breakdown product of the major membrane component phosphatidylcholine. Chk-α is being actively investigated as a target for antitumor therapy.[26,27] We previously found that a combination of siRNA-chk transfection and 5-FU treatment achieved a greater reduction of cell viability in malignant human mammary epithelial cells compared to nonmalignant ones.[28]

Noninvasive ^{1}H MRI detection of nanoplex delivery was confirmed by fluorescent imaging and microscopy. Down-regulation of Chk-α by the siRNA was detected through decreased tCho observed by noninvasive ^{1}H MRSI, a technique routinely used in the clinic, and further validated by immunoblotting. Conversion of 5-FC to 5-FU was determined *in vivo* by ^{19}F MRS. Therapeutic response was evaluated from changes in tumor growth and histology.

This nanoplex strategy can be expanded to down-regulate multi-drug-resistant pathways or repair enzymes and increase the efficiency of chemo- or radiation therapy.

RESULTS

Nanoplex Synthesis and Characterization. The synthesis of the nanoplex (nanoplex **11**) is outlined in Figure 1. Briefly, treatment of Cy5.5-NHS esters and DOTA-NHS ester with poly-L-lysine (PLL) gave **1**. After complexation with Gd^{3+}, compound **2** was functionalized with *S*-acetylthioacetate and hydrazine to give **4**. Meanwhile, branched PEI was labeled with rhodamine and polyethyl glycol (PEG) (2.0 kDa). The cografted polymer bPEI-PEG **5** was labeled with benzaldehyde to give **6**. Conjugation of equivalent **4** and **6** resulted in the PLL-PEI copolymer **7**. The reduction of *S*-acetylthioacetate in **7** to a sulfhydryl group gave **8**. Treatment of bCD[11] with *N*-[e-maleimidocaproyloxy]succinimide ester (EMCS) gave **9**. Cross-linking of **9** with **8** gave bCD-111 (**10**). Finally, condensation of siRNA-chk with **10** provided nanoplex **11**.

The molar ratio of bCD/PEI/PLL in vector bCD-111 (**10**) was measured as 1/1.05/1.2. The molecular weight of **10** was determined as 366 kDa (Supporting Information, Figure S1), and its average diameter and zeta potential were 55 nm and 0.9 mV, respectively, at pH 7.4 (Supporting Information, Figure S2). The longitudinal relaxivity r_{1p} of **10** was 16.6 mM^{-1} s^{-1} at 9.4 T and 25 °C (Supporting Information, Figure S3). Kinetic studies demonstrated that **10** and unmodified bCD have similar Michaelis−Menton constant K_m values to both substrates of cytosine and 5-FC (Supporting Information, Table S1). Compared to the unmodified bPEI, the IC_{50} of **10** in MDA-MB-231 cells increased 23 times to 4.8 μM (Supporting Information, Figure S4). **10** also showed high enzymatic stability and efficiently converted 5-FC to 5-FU even 24 h after internalization (Supporting Information, Figure S5). As shown in Figures S6 and S7 in Supporting Information, nanoplex **11** remained intact at an N/P ratio greater than 20 and the siRNA-chk encapsulated in nanoplex **11** was well-protected in 70% fresh mouse serum even 8 h after incubation. Immunoblot studies also clearly demonstrated the N/P ratio-dependent Chk silencing efficacy in MDA-MB-231 cells (Supporting Information, Figure S8).

Cellular and Molecular Characterization of Combined siRNA and Prodrug Strategy. Efficient cellular uptake of nanoplex **11** in live MDA-MB-231 cells was demonstrated with confocal fluorescence microscopy. After 30 min incubation, the predominant attachment of the nanoplex to the cell membrane was likely due to the nonspecific electrostatic interaction between the positively charged nanoplex and the negatively charged cell surface proteoglycans (Figure 2A).[30,31] Distinct fluorescent vesicular structures were observed in the cytoplasm after incubation for 4 h, while fluorescence at the cell membrane diminished, suggesting that the nanoplex was internalized through endocytosis (Figure 2B).[32] Intracellular delivery of the nanoplex was verified by yellow vesicular structures resulting from colocalization of red fluorescence from rhodamine labeled in the PEI vector and green fluorescence from FITC labeled in the siRNA-chk. Cytosolic release of encapsulated siRNA-chk from nanoplex **11** was evident from the diffuse green stain observed in areas adjacent to the yellow vesicular structures at 4 h after treatment (enlarged area 2, Figure 2B). Cytosolic release of the siRNA-chk was more apparent at 24 h after the nanoplex uptake (Figure 2C). In some cells, the green stain occupied the entire cytoplasm including the nuclear area (enlarged area 3, Figure 2C). These live cell fluorescence images indicated that nanoplex **11** not only efficiently delivered encapsulated siRNA-chk into cancer cells but also possessed the ability to release the siRNA-chk into the cytoplasm, which was essential for the siRNA to down-regulate the message.

The transient transfection efficiency of nanoplex **11** in MDA-MB-231 cells was evaluated with immunoblotting (Figure 3A). Effective Chk down-regulation by the nanoplex compared with negative (oligofectamine alone) and positive (oligofectamine/siRNA-chk lipoplex) controls with the same siRNA-chk concentration was

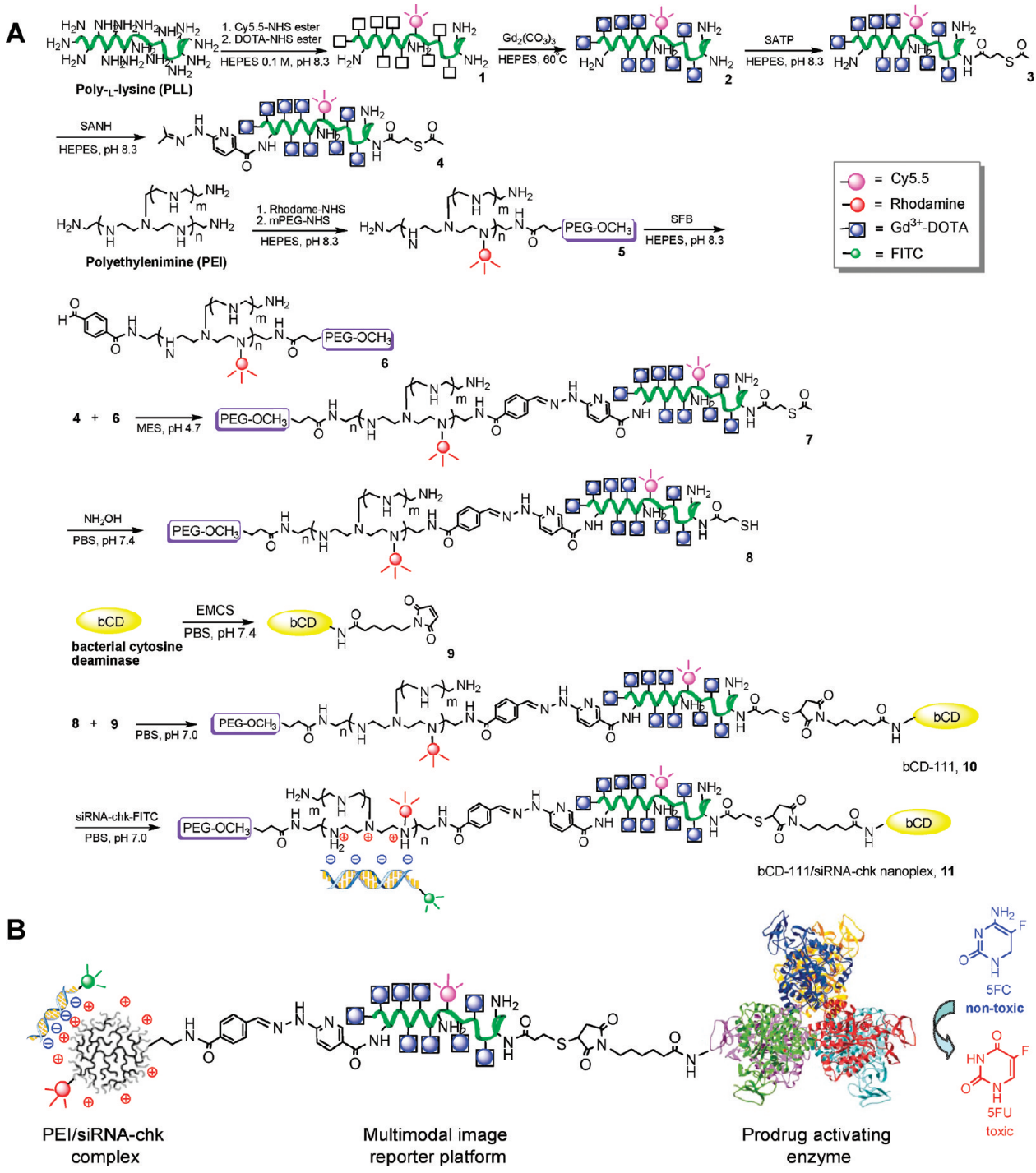

Figure 1. (A) Synthetic procedure of nanoplex 11. (B) Schematic structure of nanoplex 11.

observed. Nanoplex **11** showed a siRNA concentration-dependent Chk down-regulation efficacy. Notably, Chk silencing was observed for siRNA-chk concentrations as low as 20 nM.

Chk levels in tumors treated with PBS, **10**/scrambled siRNA nanoplex, or nanoplex **11** were substantially lower in tumors treated with nanoplex **11** (300 mg/kg, N/P = 50, i.v.) for 24 and 48 h (Figure 3B). We also investigated intratumoral Chk levels after the combined strategy for 48 h (5-FC was delivered 24 h after nanoplex **11**); however, no further reduction of Chk levels was observed.

Imaging of Nanoplex 11 *In Vivo* and *Ex Vivo*. Both *in vivo* optical imaging and MRI studies demonstrated efficient intratumoral delivery of nanoplex **11** (300 mg/kg *via* i.v.) in tumors. *In vivo* dynamic NIR fluorescence imaging showed the uptake of nanoplex **11** in the tumor as early as 15 min post-i.v. injection (Figure 4A). NIR fluorescence intensities in tumors reached a maximum value of $7.4 \pm 0.6 \times 10^9$ ps^{-1} cm^{-2} sr^{-1} ($n = 3$, Figure 4B) at

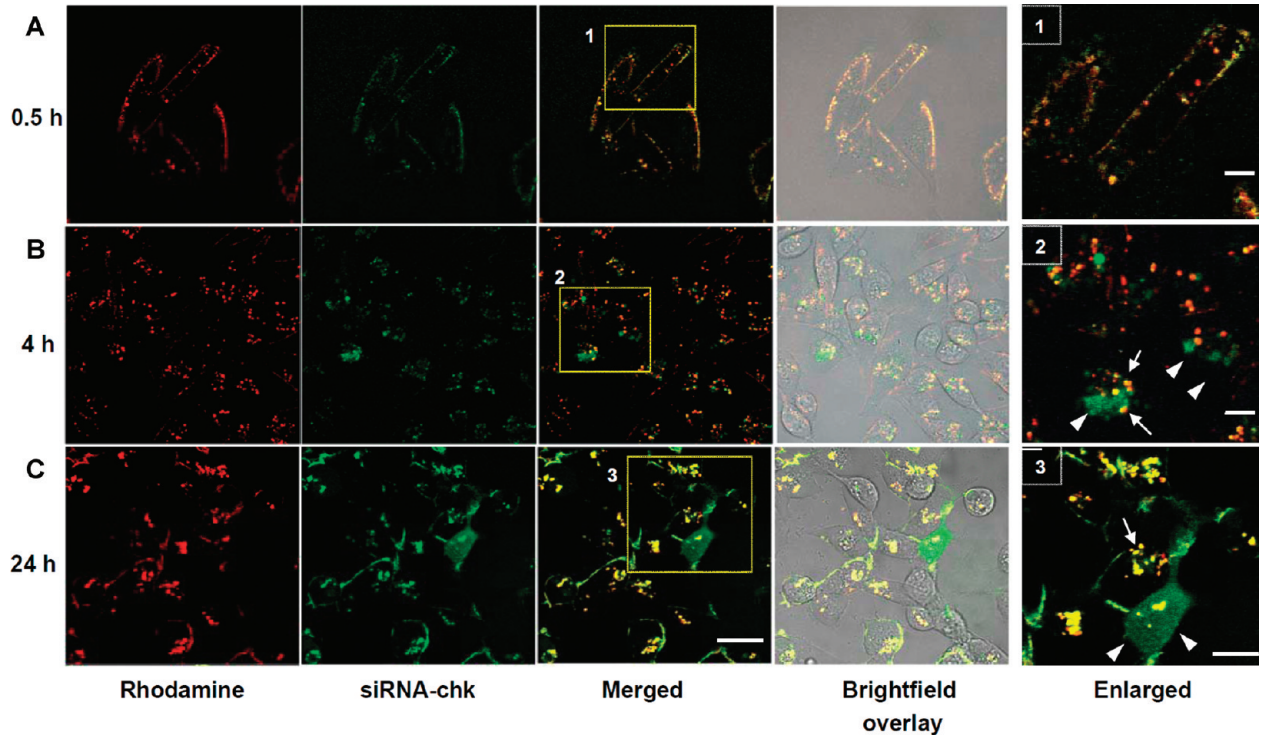

Figure 2. Confocal fluorescent and brightfield microscopic images of live cells treated with the nanoplex 11 for 0.5 (A), 4 (B), and 24 h (C). The yellow color in merged fluorescence images represents colocalization between FITC and rhodamine and indicates internalization of the nanoplex. The diffuse green staining is from siRNA-chk released in the cytosol. Scale bar, 15 μm. Arrows mark vesicular delineation of the nanoplex, while arrow heads mark the released siRNA-chk. Scale bars represent 5 μm in the enlarged area.

48 h post-injection. The T/N ratio also attained a maximum value of 5.6 ± 0.5 at 48 h post-nanoplex injection (n = 3, inset of Figure 4B).

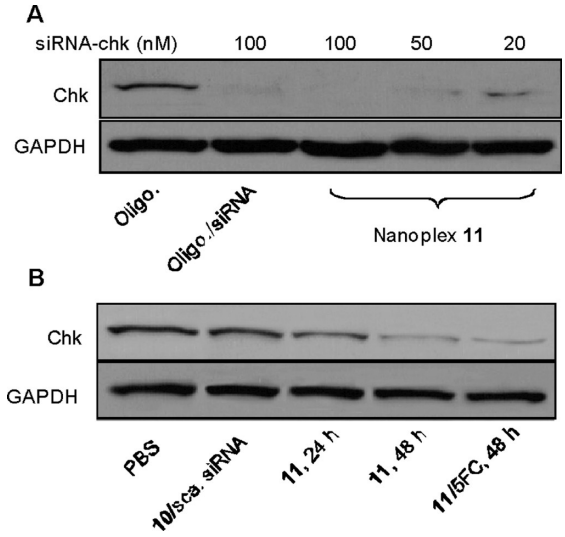

Figure 3. (A) Immunoblots showing siRNA concentration-dependent Chk down-regulation efficiency of nanoplex 11 (N/P = 50) in cultured cells. Commercial transfection agents oligofectamine and oligofectamine/siRNA-chk lipoplex (100 nM siRNA-chk) were used as negative and positive controls. GAPDH protein was used as loading control. (B) Chk levels in tumors treated with nanoplex 11 (300 mg/kg, N/P = 50, i.v.) for 24 and 48 h were substantially lower than in tumors treated with 10/scrambled siRNA nanoplex (300 mg/kg, N/P = 50, i.v.) or PBS alone. No further reduction of Chk levels was observed after the combined treatment for 48 h (5-FC was delivered 24 h after nanoplex 11 injection).

Ex vivo white light, fluorescence, and color-coded fluorescence images of tumor sections obtained at 4, 24, and 48 h following i.v. injection of the nanoplex are shown in Figure 4C. A heterogeneous intratumoral distribution pattern of the nanoplex was observed in all tumor sections, and the degree of colocalization between the fluorescence from rhodamine (PEI) and FITC (siRNA) decreased with time after nanoplex injection. These *ex vivo* fluorescence images confirmed that the encapsulated siRNA-chk was released from the nanoplex within 24−48 h post-injection.

Biodistribution data of nanoplex **11** obtained at 4, 24, and 48 h post-injection in tumor-bearing mice are shown in Figure 4D. The nanoplex predominantly accumulated in liver, kidney, lung, spleen, and tumor at 4 h after i.v. injection. Concentration of the nanoplex in the kidney, lung, and spleen decreased gradually but increased in the liver and tumor at 24 h post-injection. At 48 h, the normalized fluorescence intensity continually decreased in all normal tissues but peaked to the highest observed value in the tumor (n = 4, 5.7 ± 0.4 normalized to muscle).

Representative *in vivo* high-resolution T_1-weighted MR images and quantitative T_1 maps of a tumor before and after i.v. administration of nanoplex **11** (300 mg/kg) are shown in Figure 5A. Tumor regions with MR signal enhancement were observed immediately after injecting the nanoplex. Within 60 min of injection, the enhancement slowly diffused from the periphery to the interior of the tumor. By 24−48 h, it was mainly localized

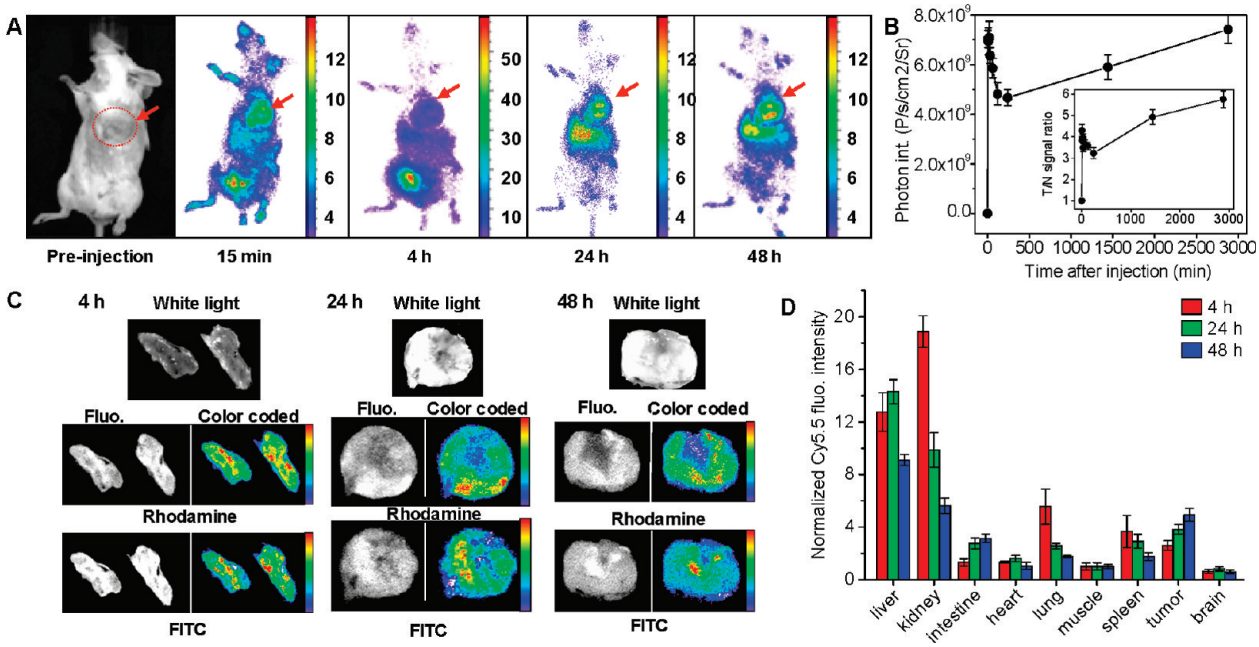

Figure 4. (A) Dynamic *in vivo* NIR optical imaging of tumor-bearing mice before and after i.v. injection of nanoplex 11 (N/P = 50). Red arrow denotes tumor location. (B) Time course of *in vivo* fluorescent intensities in tumor xenografts. Inset panel demonstrates the time course of average fluorescent intensity ratio (T/N) between the tumor and mouse body. T/N values were normalized to preinjection values. Data are expressed as mean ± SD (n = 3). (C) Representative *ex vivo* white light, fluorescence (gray scale), and color-coded fluorescence images of tumor sections at 4, 24, and 48 h post-injection (i.v.) of nanoplex (N/P = 50). Rhodamine fluorescence identified the distribution of PEI, while the FITC fluorescence identified the location of siRNA-chk. (D) Biodistribution of nanoplex 11 in tumor-bearing mice at 4, 24, and 48 h post-injection. Fluorescent intensities were normalized to that of muscle. Data are expressed as mean ± SD (n = 3).

within the central region of the tumor. MR signal enhancement in the T_1-weighted images was further confirmed as a decrease of T_1 values in the quantitative T_1 maps (lower panel in Figure 5A). The time-dependent average T_1 values of the tumor presented in Figure 5B demonstrate that T_1 values decreased significantly from 2127 ± 30 ms before injection to 1652 ± 21 ms (mean ± SD, average 22% reduction, n = 5, P = 0.0029) at 60 min post-injection. After that, the T_1 values increased slowly, but a reduction of 18% remained (1743 ± 52 ms, n = 5, P = 0.0023) at 48 h post-injection.

Real-Time Noninvasive Imaging of Therapeutic Response *In Vivo*. Evidence of the enzymatic activity of nanoplex **11** localized in the tumor was confirmed by monitoring the conversion of 5-FC to 5-FU by noninvasive ^{19}F MRS (Figure 5C). The nanoplex demonstrated high enzymatic activity even 24 h after tumor localization. As shown in Figure 5C, only a single 5-FC peak was detected immediately after prodrug administration. A peak at 3.4−3.8 ppm from F-Nucl (FU-derived fluoronucleotides and FU-derived fluoronucleosides), which are the active metabolites of 5-FU that inhibit cancer cell replication,[33,34] was apparent from 1 h onward following 5-FC injection. Another peak at 1.4 ppm from 5-FU increased slowly 2 h post-prodrug injection. The 5-FC peak intensity decreased with time, consistent with the conversion of the prodrug to the active drug by bCD.

In vivo intratumoral Chk down-regulation induced by nanoplex **11** was noninvasively evaluated by measuring tCho levels with ^{1}H MRSI. Representative tCho maps and color-coded tCho intensity maps overlaid with corresponding T_1-weighted images of a tumor before and at 24 and 48 h post-injection of the nanoplex (300 mg/kg, N/P = 50, i.v.) are shown in Figure 5D. Prior to injection, tCho was detected almost over the entire tumor. However, tCho decreased within 24 h post-injection, and by 48 h, tCho was localized to a thin peripheral rim. On average, tCho levels decreased to 35 and 34%, respectively, at 24 and 48 h post-injection compared to pretreatment values (n = 4, P = 0.0049).

Therapeutic Efficacy of Image-Guided Combined siRNA and Prodrug Strategy *In Vivo*. On the basis of the biodistribution and imaging data, the prodrug was injected 24 h after the nanoplex administration to achieve high therapeutic efficacy and low systemic toxicity. In contrast to the average tumor doubling time of 5.5 days in mice treated with PBS only or with **10**/scrambled siRNA nanoplex, an average tumor doubling time of 10 and 18 days was observed in mice treated with nanoplex **11** alone or treated with the enzyme/prodrug strategy alone, respectively. The combined prodrug/siRNA strategy, however, resulted in an average tumor doubling time of 35 days (Figure 6A). A slight body weight loss (≈5%) was observed in mice treated with the combined treatment strategy, nanoplex **11** alone or **10**/5-FC alone (Figure 6B). Mice recovered original body weights within one week.

The therapeutic response in tumors was additionally evaluated by histology. As shown in Figure 6C, gross necrosis was not detected in control tumors

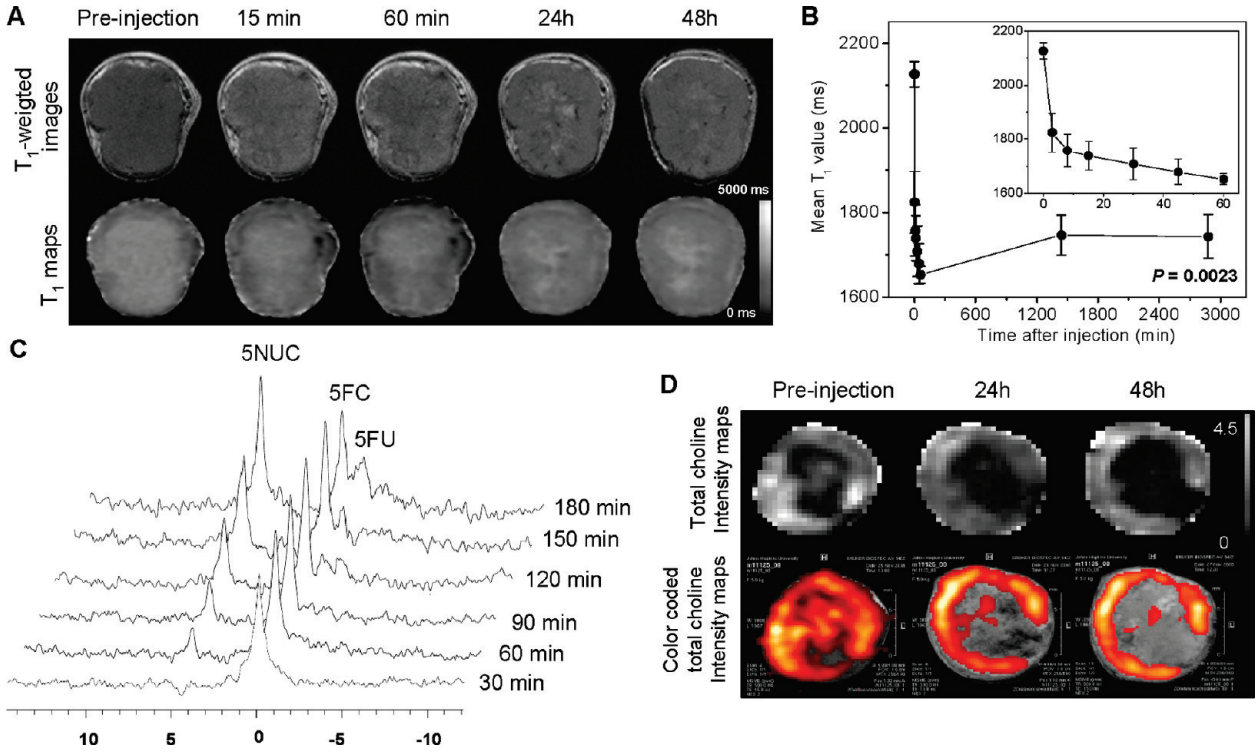

Figure 5. (A) Representative *in vivo* T_1-weighted MR images (top panel) and quantitative T_1 maps (bottom panel) of a tumor (400 mm^3) pre- and post-injection of nanoplex 11 (300 mg/kg, i.v.). (B) Time-dependent mean T_1 values of tumors ($n = 4$) pre- and post-injection of nanoplex 11; a significant decrease of T_1 ($P < 0.0023$) was observed up to 48 h. Inset panel shows the T_1 variation within the first 60 min of injection. (C) *In vivo* ^{19}F MRS demonstrated efficient conversion of prodrug 5-FC to 5-FU and its metabolites F-Nucl by nanoplex 11 localized in the tumor. 5-FC (200 mg/kg i.v. and 250 mg/kg i.p.) was injected at 24 h after nanoplex injection. (D) Representative *in vivo* tCho maps and color-coded tCho intensity maps overlaid on corresponding T_1-weighted images of a tumor before and at 24 and 48 h after nanoplex injection (300 mg/kg, i.v.).

treated with PBS alone or with scrambled siRNA in the nanoplex. In contrast, a large necrotic area (≈61 ± 12%, mean ± SD, $n = 4$) was observed at 48 h after the image-guided combined treatment. Necrosis was also detected in tumors treated with nanoplex **11** alone for 48 h (≈23 ± 7%, $n = 3$) and tumors treated with bCD-111 **10**/prodrug (≈40 ± 8%, $n = 3$, prodrug 5-FC injected at 24 h post-bCD-111 administration). No evidence of necrosis was found in the liver or kidney after combined treatment.

Kidney and Liver Function. Serum creatinine levels were 0.4 mg/dL in both control mice and 0.3 ± 0.1 mg/dL (mean ± SD) in the treated mice (normal range 0.3−1 mg/dL). Aspartate aminotransferase (AST) levels were 40 ± 4.2 U/L in control mice and 200 ± 77.8 U/L in treated mice (normal range 50−300 U/L). Alanine aminotransferase (ALT) levels were 28.5 ± 2.1 U/L in control mice and 88.5 ± 34.6 U/L in treated mice (normal range 20−80 U/L). Of the three enzymes, only ALT levels were slightly higher than the normal range. These data together with the absence of mouse body weight loss suggest that nanoplex **11** was well-tolerated *in vivo*.

DISCUSSION

Here, in proof-of-principle studies, we have demonstrated the feasibility of noninvasive molecular imaging guided delivery of siRNA and a prodrug enzyme together with noninvasive detection of target gene down-regulation and conversion of the prodrug. Both MRI and optical imaging reporters were incorporated in the nanoplex: MRI for clinical translatability and optical reporters for microscopy of cells and tissues at subcellular resolution. The NIR fluorophore Cy5.5 increased the sensitivity and quantification accuracy of optical imaging because of low tissue autofluorescence and higher penetration depth. *In vivo* ^{1}H MRI, ^{19}F MRS, ^{1}H MRSI, and optical imaging showed efficient intratumoral delivery of the nanoplex, down-regulation of the target gene, and formation of the prodrug enzyme-activated cytotoxic drug. While further optimization of dose and dose timing is required, the additive therapeutic effect achieved by the combined siRNA and prodrug enzyme strategy was evident from significant tumor growth delay and extensive necrosis.

While previous studies have reported the use of imaging to detect siRNA delivery,[35−37] here, noninvasive imaging was used not only to monitor delivery of the therapeutic prodrug enzyme and siRNA and time prodrug administration but also to evaluate, in real time, down-regulation of the message and activity of the prodrug enzyme.

The nanoplex met several criteria to achieve this multipurpose ability and maintain low cytotoxicity and biodegradability *in vivo*. The prodrug activating enzyme

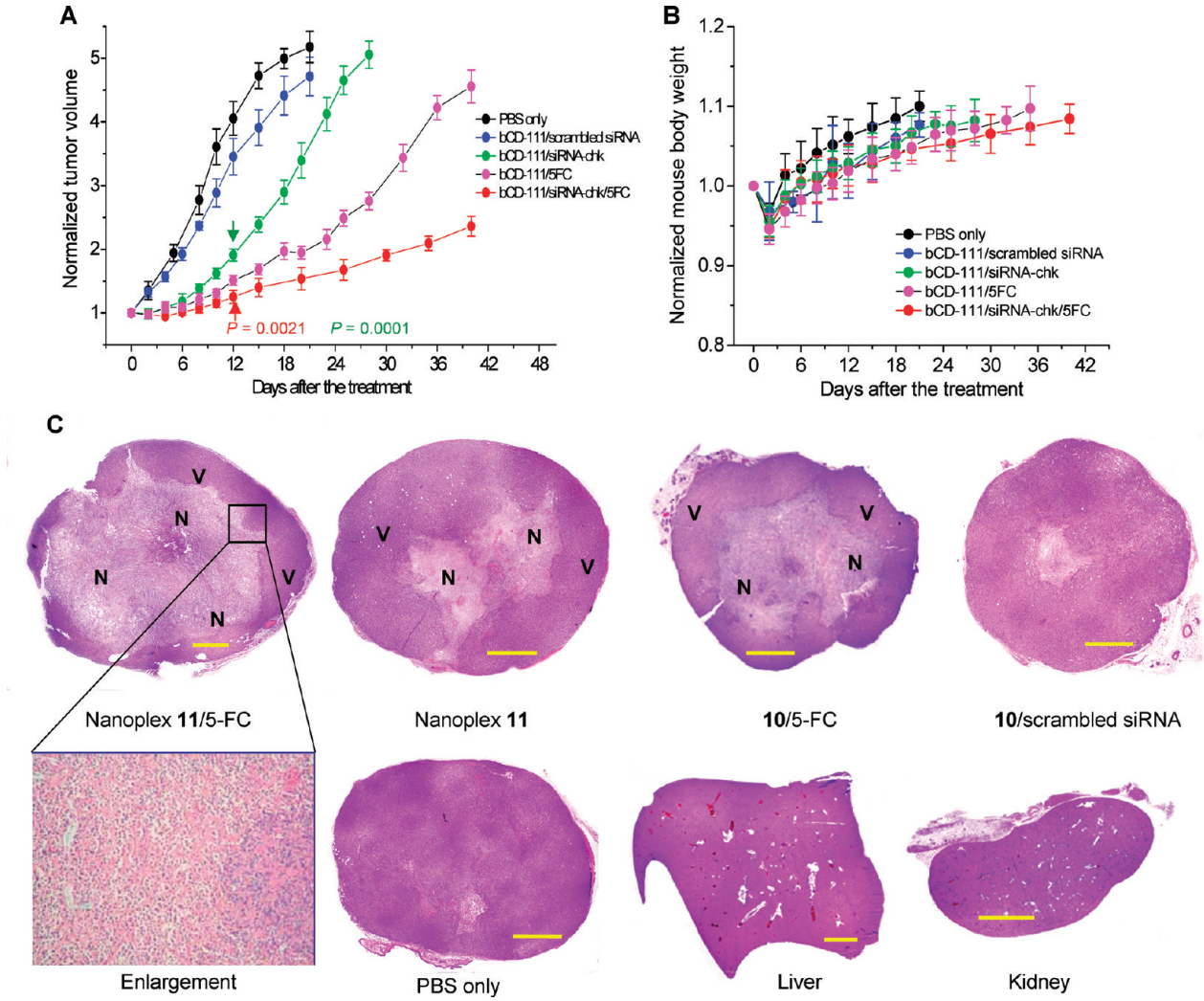

Figure 6. (A) Growth curves of tumors treated with PBS only ($n = 3$), a single dose of 10/scrambled siRNA nanoplex ($n = 3$), a single dose of nanoplex 11 ($n = 3$), a single dose of 10 ($n = 3$) followed by 5-FC (450 mg/kg) administered at 24 h after 10 injection and a single dose of nanoplex 11 ($n = 4$) followed by 5-FC (450 mg/kg) administered at 24 h after nanoplex injection. All nanoplexes 11 or 10 were injected i.v. at a dose of 300 mg/kg and N/P ratio of 50. Values are mean ± SD. Arrows point to the earliest significant difference (two tailed) compared to mean volumes of tumors treated with PBS only. (B) Time course of normalized mouse body weight after the corresponding treatments as described in panel A. (C) Representative microscopy images of H&E stained histological sections obtained at 48 h after treatment with top panel going from left to right, nanoplex 11 and prodrug 24 h later, nanoplex 11 alone, 10 and prodrug 24 h later, and 10/scrambled siRNA nanoplex. The bottom panel shows, going from left to right, a magnified view (20×) of marked area, tumor treated with PBS only for 48 h, liver, and kidney sections. Purple hematoxiphilic regions (V) indicate viable tumor tissues, and eosinophilic areas indicate tumor necrosis (N). Scale bar: 1.0 mm.

bCD, selected because of its high stability,[12] maintained high enzymatic activity after conjugation. PLL as an imaging reporter carrier provided numerous primary amines to conjugate to multimodal imaging reporters[13] with a high payload to improve sensitivity and spatial resolution of the images. Additionally, since PLL is biodegradable, the labeled Gd^{3+}-DOTA was rapidly excreted, with minimal tissue accumulation and associated side effects.[38] Synthetic polymer PEI was chosen as the siRNA delivery vector because of its buffering effect,[39] which resulted in endosomal release of endocytosed siRNA into the cytoplasm. To overcome the toxicity of cationic PEI that results from interactions with nontargeted blood components or vessel endothelia,[40,41] hydrophilic PEG was labeled to PEI to partially shield the positive charges on the PEI surface and reduce intra/intermolecular aggregation.[40] The enhanced enzymatic stability of **10** *in vivo* and *in vitro* may be due to its positive charge that accelerated cellular uptake and blocked proteolysis of bCD.[32] Other than a modest increase of serum ALT levels, neither serum creatinine nor serum AST levels were outside the normal range in nanoplex injected mice.

The higher permeability of tumor vasculature allowed the nanoplex to leak out extensively in tumors but not normal tissue.[42] Tumor specificity may have also increased because of facilitated association between the cationic nanoplex and the negatively charged sulfated proteoglycans that are overexpressed on MDA-MB-231 cell membranes.[43] The 24 h time window was selected for prodrug administration after nanoplex administration because imaging and biodistribution stud-

ies demonstrated that the T/N ratio of the nanoplex was high at this time point and that significant down-regulation of Chk-α had occurred by this time.

A fairly heterogeneous distribution of the nanoplex was observed in the tumor. At 15 min, the nanoplex was localized more at the tumor periphery, but by 60 min, it had diffused into the central region of the tumor. The distribution of tCho was heterogeneous even before the nanoplex injection. After the combined prodrug and siRNA therapy, the overall tCho level decreased significantly. However, a thin rim of cancer cells in the peripheral region of the tumor still exhibited high tCho. It is possible that a combination of the nanoplex treatment with radiation therapy may eliminate this viable rim. In future studies, it will be important to investigate the relationship between the change in T_1 and the decrease of tCho, using this platform system, since the siRNA-mediated down-regulation of choline kinase is directly reflected by the change in tCho. This may allow detection of delivery and prediction of the action any siRNA of choice, using T_1 measurements alone.

The siRNA-chk treatment and prodrug strategy alone did result in an increase of tumor doubling time, as well as an increase of necrosis. This was anticipated because down-regulating Chk-α has been previously observed to decrease cell viability,[28] and the formation of 5-FU in the tumor following treatment with the prodrug strategy alone will result in cell death, as previously observed.[13] The combined siRNA and prodrug strategy, however, resulted in a significantly longer tumor doubling time than a single treatment of either the prodrug strategy or siRNA-chk treatment given alone. The longer growth delay was consistent with large necrotic areas detected in tumors treated with the combined strategy. Necrosis in tumor sections was more extensive than nanoplex-containing regions detected in T_1-weighted images, suggesting that local diffusibility of 5-FU resulted in a strong "bystander" effect.[44]

The biodistribution studies demonstrated significant accumulation of the nanoplex in the liver and kidney. However, since down-regulation of Chk-α, the siRNA target selected, does not affect nonmalignant cells,[28] this component of the nanoplex did not pose a significant problem. The other concern is the 5-FU generated by bCD in these organs from injected 5-FC. The liver contains high levels of dihydropyrimidine dehydrogenase, which rapidly catabolizes 5-FU to dihydrofluorouracil.[45] Liver or kidney necrosis was not observed previously[13] or in the current study.

Image-guided combined siRNA and prodrug enzyme treatment has significant potential to improve therapeutic efficacy and minimize normal tissue damage. In these proof-of-principle studies, a single dose of the siRNA prodrug enzyme containing nanoplex together with the prodrug resulted in a 6-fold increase of tumor doubling time. Choosing siRNA targeting a repair or resistance pathway or enzyme, or multiple pathways/enzymes, may achieve even better growth control in combination with prodrug enzyme treatment and radiation therapy.[46]

METHODS

siRNA. The siRNA-chk duplex directed against the sequence of human Chk-α (sense: 5′-CAUGCUGUUCCAGUGCUCCUU-3′ and antisense: 5′-GGAGCACUGGAACAGCAUGUU-3′), and the scrambled siRNA ON-TARGET*plus* were purchased from Dharmacon.

Cell Lines. MDA-MB-231 human breast cancer cells (ATCC) were cultured as recommended by the supplier.

Immunoblots. Intratumoral Chk levels in cells and tumors before and after treatment were characterized by Western blot analyses using a custom-designed antibody for Chk-α.[29] Tumors were excised, weighed, and ground at selected time points after the treatments. The tissue powder was added to a RIPA buffer supplemented with protease inhibitors and homogenized. After centrifugation at 10 000*g* for 10 min, the clear supernatant was collected and the protein concentration was calculated.

Mouse Model and Tumor Implantation. All *in vivo* studies were compliant with institutional guidelines established by the Institutional Animal Care and Use Committee of Johns Hopkins University. MDA-MB-231 human breast cancer cells (2×10^6) were inoculated in the upper left thoracic mammary fat pad of female severe combined immuno-deficient (SCID) mice. Tumors used were approximately 300 mm^3. Mice were anesthetized with a mixture of ketamine (25 mg/kg) and acepromazine (2.5 mg/kg) injected intraperitoneally (i.p.).

Confocal Laser Scanning Fluorescence Microscopy. Fluorescence microscopic images of live cells were generated on a Zeiss LSM 510 META confocal laser scanning microscope (Carl Zeiss). A 63× oil immersion lens was used to collect 6−10 scanning layers from a depth of 0.8 mm. The rhodamine label in PEI was excited with a 543 nm laser, and the emission was detected by a photomultiplier tube using a 560 nm band-pass filter. The FITC label in siRNA-chk was excited with a 488 nm laser and the emission detected with a secondary photomultiplier using a 505 to 550 nm band-pass filter.

***In Vivo* MRI.** All MR (imaging and spectroscopy) studies were performed noninvasively *in vivo* on a 9.4T MR spectrometer (Bruker) using a solenoidal coil placed around the tumor. In the MRI studies, multislice relaxation rates (T_1^{-1}) were obtained by a saturation recovery method combined with fast T_1 SNAPSHOT-FLASH imaging (flip angle of 10°, echo time of 2 ms), as previously described.[13] Images of 4−6 slices (slice thickness of 1 mm) acquired with an in-plane spatial resolution of 0.125 mm (128 × 128 matrix, field of view of 16 mm, NA = 8) were obtained for three relaxation delays (100 ms, 500 ms, and 1 s). A fully relaxed Mo map with a recovery delay of 10 s was acquired once at the beginning of the experiment. Images were obtained before and at time points after intravenous administration of the nanoplex delivered through a catheterized tail vein. T_1 relaxation maps were reconstructed from data sets for three different relaxation times and the Mo data set on a pixel by pixel basis.

***In Vivo* ^{19}F MRS.** ^{19}F MR spectra from the tumor were acquired using a one pulse sequence (flip angle, 60°; repetition time, 0.8 s; number of averages, 2,000; spectral width, 10 kHz).[13]

***In Vivo* ^{1}H MRSI.** MRSI was performed using a 2D chemical shift imaging (CSI) sequence. Water-suppressed MRSI was performed on a 4 mm thick central slice, with an in-plane resolution of 1 mm × 1 mm per pixel using a 2D CSI sequence with VAPOR water suppression and the following parameters: echo time (TE) of 120 ms, repetition time (TR) of 1000 ms, field of view (FOV) of 1.6

cm × 1.6 cm, phase encode steps of 16 (16 × 16 voxels), number of scans (NS) 8 for 2D CSI, block size 1024, and sweep width of 4000 Hz. Water-unsuppressed reference MRSI was acquired from the same tumor slice as the water-suppressed MRSI, but with TE = 20 ms and NS = 2, and all other parameters the same. Spectroscopic images of the tCho signal at 3.2 ppm and the water signal at 4.7 ppm were generated from the MRSI data sets using an in-house IDL program and analyzed using the freeware program ImageJ 1.37v (http://rsb.info.nih.gov/ij/).

***In Vivo* Optical Imaging.** *In vivo* optical images were acquired with an IVIS 200 scanner (Caliper) as previously described.[13] Time-dependent fluorescence intensities in regions of interest (ROIs) were quantified by using Living Image 2.5 software (Caliper). Tumor/normal tissue ratio (T/N) was calculated by comparing the average Cy5.5 fluorescence intensities in the tumor ROI and the whole mouse body. All *in vivo* fluorescence images were acquired using 0.1 s exposure time under the Cy5.5 channel (FOV 6.4 or 12.8 cm; f/stop, 4; bin, high resolution), and the fluorescence intensity was scaled as a unit of ps^{-1} cm^{-2} sr^{-1}.

Biodistribution. Mice were sacrificed, and the tumor and other organs were excised and carefully sliced to a thickness of 3.0 mm to minimize depth-dependent nonlinear fluorescence emission.[13] Tissue slices were imaged with an IVIS 200 scanner (Caliper). Fluorescence intensities of tissue sections were quantified by ImageJ software (NIH, Bethesda, MD) and normalized to that of muscle. Mean relative fluorescent intensities were obtained by averaging at least five FOV for different sections from the same organ.

***In Vivo* Antitumor Effect.** To investigate the therapeutic response of the combined strategy, nanoplex **11** (300 mg/kg i.v.) was injected in mice ($n = 6$) followed by a dose (450 mg/kg) of 5-FC (administered as 200 mg/kg i.v. and 250 mg/kg i.p.) at 24 h after the nanoplex injection. As controls, mice ($n = 5$) were injected with nanoplex **11** (300 mg/kg i.v.) without prodrug administration or with conjugate **10** (300 mg/kg i.v., $n = 3$) followed by a dose (450 mg/kg) of 5-FC (administered as 200 mg/kg i.v. and 250 mg/kg i.p.) after 24 h or with nanoplex **11** (300 mg/kg i.v., $n = 3$) alone, or with PBS (250 μL i.v., $n = 3$) only. Tumor volumes and body weights of mice were measured on the day of administration and subsequently every 2−3 days until tumor volumes reached 1.0 cm^3.

Kidney and Liver Function. Studies were performed to evaluate kidney and liver function following nanoplex injection. Serum creatinine levels and serum ALT and AST levels were evaluated by the Johns Hopkins University School of Medicine Phenotyping Core Facility, from spectrophotometric measurements obtained with an automated Vet Ace Clinical Chemistry system (Alfa Wasserman Diagnostic Technologies LLC, NJ), which is an automated benchtop random access analyzer that provides quantitative measurements of constituents in blood and serum. Serum was obtained from control mice ($n = 2$) and treated mice ($n = 2$) 48 h after injecting the nanoplex.

Histological Evaluation. Tumors were fixed in formalin, sectioned at 5 μm thickness, and stained with hematoxylin and eosin. At least three 5 μm thick sections were obtained form each tumor and analyzed. Three to four tumors from each group were analyzed. Necrotic cells were identified by pyknotic nuclei or lack of nuclei that resulted in a decrease of purple staining of chromatin by hematoxylin, leaving a primarily pale pink eosinophilic staining of the cytoplasm in necrotic areas. Percent necrosis in the tumor sections was determined by obtaining a ratio of necrotic to the total tumor area in each section from images acquired with a 2× objective using ImageJ software.

Statistical Analysis. Values are presented as mean ± SD of at least three experiments. Statistical differences were evaluated with Student's *t* test (Excel 2002, Microsoft); $P < 0.05$ (two tailed) was considered significant.

Acknowledgment. This work was supported by NIH R01CA138515 and P50 CA103175. We thank Drs. M. Neeman, V. Raman, and P. Senter for helpful discussions, and Drs. Y. Kato, N. Mori, B. Krishnamachary, and K. Glunde for technical assistance. We thank Dr. Barry Stoddard for providing the bCD cDNA. We gratefully acknowledge support from Dr. J.S. Lewin. C.L. gratefully acknowledges support from Prof. Y.Z. Zhu, the Chinese National Science Foundation (30900353), and the National Science and Technology Major Project (2009ZX09310-006).

Supporting Information Available: Detailed synthesis, characterization, enzymatic kinetics, cytotoxicity, and nanoplex stability in mouse serum. This material is available free of charge *via* the Internet at http://pubs.acs.org.

REFERENCES AND NOTES

1. Hassett, M. J.; O'Malley, A. J.; Pakes, J. R.; Newhouse, J. P.; Earle, C. C. Frequency and Cost of Chemotherapy-Related Serious Adverse Effects in a Population Sample of Women with Breast Cancer. *J. Natl. Cancer Inst.* **2006**, *98*, 1108–1117.
2. Ladewski, L. A.; Belknap, S. M.; Nebeker, J. R.; Sartor, O.; Lyons, E. A.; Kuzel, T. C.; Tallman, M. S.; Raisch, D. W.; Auerbach, A. R.; Schumock, G. T.; *et al.* Dissemination of Information on Potentially Fatal Adverse Drug Reactions for Cancer Drugs from 2000 to 2002: First Results from the Research on Adverse Drug Events and Reports Project. *J. Clin. Oncol.* **2003**, *21*, 3859–3866.
3. Fire, A.; Xu, S.; Montgomery, M. K.; Kostas, S. A.; Driver, S. E.; Mello, C. C. Potent and Specific Genetic Interference by Double-Stranded RNA in *Caenorhabditis elegans*. *Nature* **1998**, *391*, 806–811.
4. Meister, G.; Tuschl, T. Mechanisms of Gene Silencing by Double-Stranded RNA. *Nature* **2004**, *431*, 343–349.
5. Devi, G. R. siRNA-Based Approaches in Cancer Therapy. *Cancer Gene Ther.* **2006**, *13*, 819–829.
6. Xu, G.; McLeod, H. L. Strategies for Enzyme/Prodrug Cancer Therapy. *Clin. Cancer Res.* **2001**, *7*, 3314–3324.
7. Russell, P. J.; Khatri, A. Novel Gene-Directed Enzyme Prodrug Therapies against Prostate Cancer. *Expert Opin. Invest. Drugs* **2006**, *15*, 947–961.
8. Singh, Y.; Palombo, M.; Sinko, P. J. RNAi-Mediated Silencing of Nuclear Factor Erythroid-2-Related Factor 2 Gene Expression in Non-small Cell Lung Cancer Inhibits Tumor Growth and Increases Efficacy of Chemotherapy. *Curr. Med. Chem.* **2008**, *15*, 1802–1826.
9. Jain, R. K. Transport of Molecules in the Tumor Interstitium: A Review. *Cancer Res.* **1987**, *47*, 3039–3051.
10. Fukumura, D.; Jain, R. K. Tumor Microvasculature and Microenvironment: Targets for Anti-angiogenesis and Normalization. *Microvasc. Res.* **2007**, *74*, 72–84.
11. Li, C.; Winnard, P. T., Jr.; Takagi, T.; Artemov, D.; Bhujwalla, Z. M. Multimodal Image-Guided Enzyme/Prodrug Cancer Therapy. *J. Am. Chem. Soc.* **2006**, *128*, 15072–15073.
12. Ireton, G. C.; McDermott, G.; Black, M. E.; Stoddard, B. L. The Structure of *Escherichia coli* Cytosine Deaminase. *J. Mol. Biol.* **2002**, *315*, 687–697.
13. Li, C.; Penet, M. F.; Winnard, P., Jr.; Artemov, D.; Bhujwalla, Z. M. Image-Guided Enzyme/Prodrug Cancer Therapy. *Clin. Cancer Res.* **2008**, *14*, 515–522.
14. Penet, M. F.; Mikhaylova, M.; Li, C.; Krishnamachary, B.; Glunde, K.; Pathak, A. P.; Bhujwalla, Z. M. Applications of Molecular MRI and Optical Imaging in Cancer. *Future Med. Chem.* **2010**, *2*, 975–988.
15. Glunde, K.; Jacobs, M. A.; Bhujwalla, Z. M. Choline Metabolism in Cancer: Implications for Diagnosis and Therapy. *Expert Rev. Mol. Diagn.* **2006**, *6*, 821–829.
16. Ramirez de Molina, A.; Gutierrez, R.; Ramos, M. A.; Silva, J. M.; Silva, J.; Bonilla, F.; Sanchez, J. J.; Lacal, J. C. Increased Choline Kinase Activity in Human Breast Carcinomas: Clinical Evidence for a Potential Novel Antitumor Strategy. *Oncogene* **2002**, *21*, 4317–4322.
17. Ramirez de Molina, A.; Rodriguez-Gonzalez, A.; Gutierrez, R.; Martinez-Pineiro, L.; Sanchez, J.; Bonilla, F.; Rosell, R.; Lacal, J. Overexpression of Choline Kinase is a Frequent Feature in Human Tumor-Derived Cell Lines and in Lung, Prostate, and Colorectal Human Cancers. *Biophys. Res. Commun.* **2002**, *296*, 580–583.
18. Aboagye, E. O.; Bhujwalla, Z. M. Malignant Transformation Alters Membrane Choline Phospholipid Metabolism of Human Mammary Epithelial Cells. *Cancer Res.* **1999**, *59*, 80–84.

19. Podo, F. Tumour Phospholipid Metabolism. *NMR Biomed.* **1999**, *12*, 413–439.
20. Gallego-Ortega, D.; Ramirez de Molina, A.; Ramos, M. A.; Valdes-Mora, F.; Barderas, M. G.; Sarmentero-Estrada, J.; Lacal, J. C. Differential Role of Human Choline Kinase Alpha and Beta Enzymes in Lipid Metabolism: Implications in Cancer Onset and Treatment. *PLoS One* **2009**, *4*, e7819.
21. Nelson, S. J.; Graves, E.; Pirzkall, A.; Li, X.; Antiniw Chan, A.; Vigneron, D. B.; McKnight, T. R. *In Vivo* Molecular Imaging for Planning Radiation Therapy of Gliomas: an Application of ^{1}H MRSI. *J. Magn. Reson. Imaging* **2002**, *16*, 464–476.
22. Katz-Brull, R.; Lavin, P. T.; Lenkinski, R. E. Clinical Utility of Proton Magnetic Resonance Spectroscopy in Characterizing Breast Lesions. *J. Natl. Cancer Inst.* **2002**, *94*, 1197–1203.
23. Negendank, W. Studies of Human Tumors by MRS: A Review. *NMR Biomed.* **1992**, *5*, 303–324.
24. Glunde, K.; Artemov, D.; Penet, M. F.; Jacobs, M. A.; Bhujwalla, Z. M. Magnetic Resonance Spectroscopy in Metabolic and Molecular Imaging and Diagnosis of Cancer. *Chem. Rev.* **2010**, *110*, 3043–3059.
25. Glunde, K.; Ackerstaff, E.; Mori, N.; Jacobs, M. A.; Bhujwalla, Z. M. Choline Phospholipid Metabolism in Cancer: Consequences for Molecular Pharmaceutical Interventions. *Mol. Pharm.* **2006**, *3*, 496–506.
26. Rodriguez-Gonzalez, A.; Ramirez de Molina, A.; Fernandez, F.; Ramos, M. A.; del Carmen Nunez, M.; Campos, J.; Lacal, J. C. Inhibition of Choline Kinase as a Specific Cytotoxic Strategy in Oncogene-Transformed Cells. *Oncogene* **2003**, *22*, 8803–8812.
27. Rodriguez-Gonzalez, A.; Ramirez de Molina, A.; Fernandez, F.; Lacal, J. C. Choline Kinase Inhibition Induces the Increase in Ceramides Resulting in a Highly Specific and Selective Cytotoxic Antitumoral Strategy as a Potential Mechanism of Action. *Oncogene* **2004**, *23*, 8247–8259.
28. Mori, N.; Glunde, K.; Takagi, T.; Raman, V.; Bhujwalla, Z. M. Choline Kinase Down-Regulation Increases the Effect of 5-Fluorouracil in Breast Cancer Cells. *Cancer Res.* **2007**, *67*, 11284–11290.
29. Glunde, K.; Raman, V.; Mori, N.; Bhujwalla, Z. M. RNA Interference-Mediated Choline Kinase Suppression in Breast Cancer Cells Induces Differentiation and Reduces Proliferation. *Cancer Res.* **2005**, *65*, 11034–11043.
30. Gowda, D. C.; Bhavanandan, V. P.; Davidson, E. A. Structures of O-Linked Oligosaccharides Present in the Proteoglycans Secreted by Human Mammary Epithelial Cells. *J. Biol. Chem.* **1986**, *261*, 4935–4939.
31. Gowda, D. C.; Bhavanandan, V. P.; Davidson, E. A. Structures of O-Linked Oligosaccharides Present in the Proteoglycans Secreted by Human Mammary Epithelial Cells. *J. Biol. Chem.* **1986**, *261*, 4926–4934.
32. Li, C.; Wildes, F.; Winnard, P., Jr.; Artemov, D.; Penet, M. F.; Bhujwalla, Z. M. Conjugation of Poly-L-Lysine to Bacterial Cytosine Deaminase Improves the Efficacy of Enzyme/Prodrug Cancer Therapy. *J. Med. Chem.* **2008**, *51*, 3572–3582.
33. Hamstra, D. A.; Lee, K. C.; Tychewicz, J. M.; Schepkin, V. D.; Moffat, B. A.; Chen, M.; Dornfeld, K. J.; Lawrence, T. S.; Chenevert, T. L.; Ross, B. D.; *et al.* The Use of ^{19}F Spectroscopy and Diffusion-Weighted MRI To Evaluate Differences in Gene-Dependent Enzyme Prodrug Therapies. *Mol. Ther.* **2004**, *10*, 916–928.
34. Lutz, N. W.; Naser-Hijazi, B.; Koroma, S.; Berger, M. R.; Hull, W. E. Fluoropyrimidine Chemotherapy in a Rat Model: Comparison of Fluorouracil Metabolite Profiles Determined by High-Field ^{19}F-NMR Spectroscopy of Tissues *Ex Vivo* with Therapy Response and Toxicity for Locoregional *vs* Systemic Infusion Protocols. *NMR Biomed.* **2004**, *17*, 101–131.
35. Mikhaylova, M.; Stasinopoulos, I.; Kato, Y.; Artemov, D.; Bhujwalla, Z. M. Imaging of Cationic Multifunctional Liposome-Mediated Delivery of COX-2 siRNA. *Cancer Gene Ther.* **2009**, *16*, 217–226.
36. Kim, S. H.; Jeong, J. H.; Lee, S. H.; Kim, S. W.; Park, T. G. Local and Systemic Delivery of VEGF siRNA Using Polyelectrolyte Complex Micelles for Effective Treatment of Cancer. *J. Controlled Release* **2008**, *129*, 107–116.
37. Medarova, Z.; Pham, W.; Farrar, C.; Petkova, V.; Moore, A. *In Vivo* Imaging of siRNA Delivery and Silencing in Tumors. *Nat. Med.* **2007**, *13*, 372–377.
38. Stratta, P.; Canavese, C.; Aime, S. Gadolinium-Enhanced Magnetic Resonance Imaging, Renal Failure and Nephrogenic Systemic Fibrosis/Nephrogenic Fibrosing Dermopathy. *Curr. Med. Chem.* **2008**, *15*, 1229–1235.
39. Boussif, O.; Lezoualc'h, F.; Zanta, M. A.; Mergny, M. D.; Scherman, D.; Demeneix, B.; Behr, J. P. A Versatile Vector for Gene and Oligonucleotide Transfer into Cells in Culture and *In Vivo*: Polyethylenimine. *Proc. Natl. Acad. Sci. U.S.A.* **1995**, *92*, 7297–7301.
40. Petersen, H.; Fechner, P. M.; Martin, A. L.; Kunath, K.; Stolnik, S.; Roberts, C. J.; Fischer, D.; Davies, M. C.; Kissel, T. Polyethylenimine-Graft-Poly(ethylene glycol) Copolymers: Influence of Copolymer Block Structure on DNA Complexation and Biological Activities as Gene Delivery System. *Bioconjugate Chem.* **2002**, *13*, 845–854.
41. Chollet, P.; Favrot, M. C.; Hurbin, A.; Coll, J. L. Side-Effects of a Systemic Injection of Linear Polyethylenimine−DNA Complexes. *J. Gene Med.* **2002**, *4*, 84–91.
42. Greish, K. Enhanced Permeability and Retention of Macromolecular Drugs in Solid Tumors: A Royal Gate for Targeted Anticancer Nanomedicines. *J. Drug Target* **2007**, *15*, 457–464.
43. Delehedde, M.; Deudon, E.; Boilly, B.; Hondermarck, H. Production of Sulfated Proteoglycans by Human Breast Cancer Cell Lines: Binding to Fibroblast Growth Factor-2. *J. Cell Biochem.* **1997**, *64*, 605–617.
44. Huber, B. E.; Austin, E. A.; Richards, C. A.; Davis, S. T.; Good, S. S. Metabolism of 5-Fluorocytosine to 5-Fluorouracil in Human Colorectal Tumor Cells Transduced with the Cytosine Deaminase Gene: Significant Antitumor Effects When Only a Small Percentage of Tumor Cells Express Cytosine Deaminase. *Proc. Natl. Acad. Sci. U.S.A.* **1994**, *91*, 8302–8306.
45. Longley, D. B.; Harkin, D. P.; Johnston, P. G. 5-Fluorouracil: Mechanisms of Action and Clinical Strategies. *Nat. Rev. Cancer* **2003**, *3*, 330–338.
46. Dachs, G. U.; Tupper, J.; Tozer, G. M. From Bench to Bedside for Gene-Directed Enzyme Prodrug Therapy of Cancer. *Anticancer Drugs* **2005**, *16*, 349–359.